Carbon 165 (2020) 18–25

Contents lists available at ScienceDirect

Carbon

journal homepage: www.elsevier.com/locate/carbon

Nano-patching defects of reduced graphene oxide by cellulose nanocrystals in scalable polymer nanocomposites

Jinhwa You [a, 1], Sukyoung Won [a, 1], Hyoung-Joon Jin [a], Young Soo Yun [b, **], Jeong Jae Wie [a, *]

[a] Department of Polymer Science and Engineering, Inha University, 100 Inha-ro, Michuhol-gu, Incheon, 22212, Republic of Korea
[b] KU-KIST Graduate School of Converging Science and Technology, Korea University, 145 Anam-ro, Seongbuk-gu, Seoul, 02841, Republic of Korea

ARTICLE INFO

Article history:
Received 12 February 2020
Received in revised form
10 April 2020
Accepted 11 April 2020
Available online 16 April 2020

Keywords:
Nano-patching
Polymer nanocomposite
Cellulose nanocrystal
Reduced graphene oxide
Gas barrier film

ABSTRACT

Reduced graphene oxide (rGO) has been widely produced by exfoliation of pristine graphite followed by oxidation and reduction. However, a number of defects can be generated during the synthesis of rGO, restricting the ability to scale-up in industrial production of defect-free rGO. The defects in rGO have limited its capacity for utilization of the full potential of the physical properties of polymer nanocomposites, such as gas and water barrier performances. Hence, this study analyzes the nano-patching of rGO defects through hydrophilic interactions of oxygen functional groups in rGO with cellulose nanocrystals (CNCs) in polyvinylidene chloride (PVDC) nanocomposites. For scalable production of defect-engineered PVDC nanocomposite barrier films, the surface energies of rGO and CNC dual nanofiller systems were regulated to prevent phase-separation of nanofillers in the PVDC matrices. The barrier properties of the PVDC/nano-patched filler composites showed drastic reduction of oxygen and water vapor transmission rates corresponding to 0.45 $cm^3\ m^{-2}\ day^{-1}$ and 0.52 $cm^3\ m^{-2}\ day^{-1}$, respectively, that decreased by 94.2% and 87.9% compared to that of the neat PVDC host. The nano-patching strategy provides novel and effective defect engineering of graphene for polymer nanocomposites.

1. Introduction

The growth of graphene on substrates by chemical vapor deposition [1] has been considered mainly for mass production as the mechanical layer-by-layer exfoliation of graphite prohibits large-scale production. The two-dimensional basal plane of graphene with its macroscopic lateral size and atomic thickness offers a wide range of applications, such as barrier properties of polymer nanocomposites [2] and electronic devices [3,4]. However, graphene exhibits low solubility in various solvents due to strong van der Waals attractions between the two-dimensional honeycomb lattices. Moreover, the dispersion of graphene nanosheets in polymer matrices is hindered when repulsive interfacial interactions exist between the polymer and graphene nanosheets, causing a large free volume at the interface [5–7].

An alternative approach is to synthesize graphene oxide (GO) by oxidizing graphite followed by the exfoliation of graphite oxide [8]. GO features stable dispersibility in water and organic solvents [7] owing to sp^3 hybridization, where hydrophilic functional groups such as epoxide and hydroxyl groups of basal planes are arranged with carbonyl and carboxyl groups at the edge planes. Reduced GO (rGO) is obtained from GO by partially recovering the sp^2 hybridized arrangement of graphene through thermal, electrochemical, or chemical reduction of oxygen functional groups [9].

However, defects can be generated during the preparation of graphene, GO, and rGO, such as Stone-Wales defects, vacancies, grain boundaries, and macroscopic defects [10]. The defective areas in two-dimensional materials can inhibit improvement of the physical properties of polymer/graphene nanocomposites. For example, unintended gas permeation into the defects in the graphene nanosheets can hinder the tortuosity of diffusion paths in polymer nanocomposite films. The gas permeability mechanism in polymer films is composed of three different steps: physical gas adhesion to the surface of the polymer film, absorption of the adhered gas molecules, and diffusion in the polymer film [11–15]. The adhesion and absorption of gas molecules affect solubility (S), which is expressed as permeability (P) by multiplication with

---

* Corresponding author.
** Corresponding author.
E-mail addresses: c-ysyun@korea.ac.kr (Y.S. Yun), wie@inha.ac.kr (J.J. Wie).
[1] These authors contributed equally to this work.

https://doi.org/10.1016/j.carbon.2020.04.024
0008-6223/

diffusivity (D), i.e., (P = S × D) [16]. Therefore, small crystal lattices of defect-free graphene nanosheets can lead to decreased gas diffusivity through the basal plane of graphene [17–19]. The minimization of graphene defects [20] and functionalization of graphene derivatives [2] have been attempted to improve the physical properties of graphene.

This study discusses a facile and effective defect engineering method of rGO by nano-patching cellulose nanocrystals (CNCs) to obtain scalable production of polyvinylidene chloride (PVDC) nanocomposite films. In principle, the defects of the two-dimensional rGO nanosheets are reinforced with needle-like high-aspect-ratio nanofillers to enhance the interfacial energy [21]. The CNCs showed nano-patching effects through hydrophilic interactions with rGO, resulting in a homogeneous dispersion of dual nanofillers in the organic co-solvents and their PVDC solution. The prevention mechanism for phase separation of dual nanofillers in the PVDC matrices will be discussed from the perspective of surface energy control by varying the weight ratio of CNC and rGO. The effects of nano-patched rGO dispersion with CNCs will be discussed with barrier properties against oxygen and water transmission, along with the dimensional and thermal stability.

2. Experimental

2.1. Sample preparation

2.1.1. Cellulose nanocrystals

Microcrystalline cellulose (MCC powder, Sigma Aldrich) was acid-hydrolyzed at 45 °C in a 64% sulfuric acid solution for 1 h (MCC:sulfuric acid = 1 g:8.75 mL) to remove amorphous regions. To terminate the acid hydrolysis reaction, the mixture was diluted with 5 L of deionized water. After 12 h of dilution, the precipitated CNCs were collected and purified by centrifugation at 9500 rpm for 30 min, followed by lyophilization at −50 °C and 0.045 mbar for 72 h.

2.1.2. Reduced graphene oxide

All GOs with their diverse lateral size were kindly supplied by JMC Corporation (Ulsan, Korea). GO was dispersed in dimethylformamide (DMF) through solvent exchange from water to DMF. The 0.1 wt% GO dispersions (20 g) were heated to 90 °C. The mixture reacted with 0.2 mL of hydrazine by vigorous stirring at 90 °C for 12 h. The obtained rGO was repeatedly rinsed with DMF, ethanol, and distilled water. The sample was lyophilized at −50 °C and 0.045 mbar for 72 h. The as-prepared rGO powder was stored in a vacuum oven at 30 °C.

2.1.3. Dual nanofillers

Dual nanofillers of CNC and rGO were prepared by varying CNC/rGO weight ratios to be 2:1, 1:1, and 1:2, which were named as 2C:1R, 1C:1R, and 1C:2R, respectively. The dispersion of the dual nanofillers was implemented in 20 g of tetrahydrofuran (THF) and DMF (60:40 w/w) co-solvent by ultrasonication for 3 min and followed by vortex-mixing for 1 min. The dispersed nanofillers were filtered, and the residual solvents were dried in a vacuum oven at 80 °C for 12 h.

2.2. Preparation of polymer nanocomposites

Ten grams of PVDC (F216 grade, $\overline{M_w} = 90{,}000$, Asahi Kasei) was dissolved in 70 g of THF:DMF (60:40 w/w) co-solvent by stirring at 60 °C for 30 min. The PVDC solution was stirred with the CNC, rGO, or nano-patched filler solutions at 60 °C for 1 h to disperse the nanofillers at 0.01, 0.05, 0.1, and 0.2 wt% loading. The 60:40 w/w THF:DMF co-solvent system was also applied to the PVDC nanocomposites with CNC or rGO single filler systems to compare with the nano-patched CNC and rGO dual filler systems. The solution of PVDC and nanofillers was precipitated into 1 L of methanol. The precipitated samples were filtered and dried in a vacuum oven at 80 °C for 7 days. The PVDC nanocomposite films were named as PVDC/CNC, PVDC/rGO, PVDC/2C:1R, PVDC/1C:1R, and PVDC/1C:2R and prepared as 3 mm × 30 mm films using a 130 °C hot press at 35 MPa for 3 min.

2.3. Preparation of coating barrier films

The blended solutions of PVDC and nanofillers were coated by a wire bar (Bar No. 7) at 70 °C on a 125 μm thick polyethylene terephthalate (PET) (Kolon Co.) substrates. After bar coating, each nanocomposite film was dried in a convection oven at 80 °C for 4 h.

2.4. Characterization

To confirm the dispersion stability of CNC, rGO, and 1C:2R nanofillers in THF/DMF co-solvent, digital images of the nanofiller solutions were obtained using a digital camera (D7200, Nikon). The optical properties of the PVDC nanocomposite films were investigated using a UV-visible spectrometer (NEO-S490, Neogen) in the wavelength range of 400–700 nm. The contact angle of PVDC and nanofillers was measured using a contact angle analyzer (PHOENIX-300, SEO). The morphologies of CNC, rGO, and 1C:2R nanofillers were confirmed by field-emission transmission electron microscopy (FE-TEM, JEM2100F, JEOL). The chemical compositions of the nanofillers were examined by X-ray photoelectron spectroscopy (XPS, PHI 5700 ESCA, Chanhassen) with monochromatic Al Kα radiation (hν = 1,486.6 eV). The Raman spectra (LabRAm HR Evolution, HORIBA) were measured using a linearly polarized 532 nm laser with 16 mW power. The thermal degradation behaviors of the nanofillers were evaluated by a thermogravimetric analyzer (TGA, Q50, TA instruments). The 5–10 mg samples were weighed and heated from 25 °C room temperature to 700 °C at a heating rate of 10 °C min^{-1} in a nitrogen atmosphere. The oxygen transmission rate (OTR) was obtained using OX-TRAN Model 2/21 (MOCON) at 23 °C and 0% relative humidity as per ASTM D3985. The water vapor transmission rate (WVTR) was obtained using Permatran-W Model 3/61 (MOCON) at 38 °C and 100% relative humidity as per ASTM F1249. The coefficient of thermal expansion (CTE) of PVDC and nanocomposites was determined using a stress-controlled dynamic mechanical analyzer (DMA, Q800, TA instruments) with a 4.3 mm (L) × 3.4 mm (W) × 23 μm (T) film from 30 °C to 80 °C at a heating rate 5 °C min^{-1} in an air atmosphere. The activation energies for thermal decomposition of PVDC and nanocomposites were measured using the TGA (Q50, TA instruments). The constant heating rate experiments were conducted in a nitrogen atmosphere from 25 °C to 900 °C at 2, 5, 10, and 20 K/min heating rates. The activation energy was calculated using the Flynn–Wall method using the temperature at 10% conversion of weight loss for each heating rate. Additional experiments confirming water vapor permeability were performed to analyze thermal stability via the Fourier-transform infrared (FT-IR, VERTEX 80 V, Bruker) spectra. The PET substrate and barrier films with a diameter of 3.5 mm were prepared. The barrier films were PET coated with PVDC, PVDC/CNC, PVDC/rGO, and PVDC/1C:2R with 0.1 wt% loading of the nanofillers. Each film was placed on a 70 ml vial with a neck diameter of 3.3 mm containing 40 °C water. The distance between water and film was 10 mm. This moisture permeability experiment was performed in a 40 °C oven for 3 days, followed by drying in a vacuum oven at 60 °C for 3 days. The FT-IR spectra before and after the water vapor permeation were measured in the spectral region of 4000-500 cm^{-1} with over 32 scans with a resolution of 4 cm^{-1}.

3. Results and discussion

3.1. Nano-patching of rGO

For the solution casting process of PVDC nanocomposites, CNC and rGO nanofillers were dispersed in THF and DMF co-solvents having a weight ratio of 1:2 and denoted as 1C:2R (Fig. 1a). The polymer solution casting process for barrier films requires a high equilibrium vapor pressure of solvents to homogeneously coat polymeric solutions on substrates. THF is one of the most widely used solvents for PVDC-based barrier films as it has high PVDC solubility and a vapor pressure of 16.999 kPa at 20 °C. After 12 h of sonication, 0.01 wt% rGO was stably dispersed initially in the THF solvent (Fig. S1a). However, the rGO nanofillers were precipitated after vortex mixing, indicating a meta-stable dispersion property. To prepare a homogenous mixture, DMF, a good solvent for rGO, was employed as a co-solvent along with THF. The contents of DMF were minimized due to its significantly low vapor pressure of 0.516 kPa at 20 °C that can induce poor coating quality by slow evaporation of the solvent. The optimal ratio of DMF to THF was investigated by increasing the DMF content from 0 to 100 w/w in the rGO-dispersed solution. A stable dispersion of rGO was achieved in the 60:40 w/w of THF:DMF mixture solution. Meanwhile, CNCs revealed poor dispersibility in pure THF, DMF, and their co-solvents (Fig. S1b). Although the CNCs seemed dispersed in the co-solvent systems after the ultrasound treatment, they agglomerated and eventually sedimented within a few hours.

For miscible dispersion of nanofillers in PVDC matrices, surface energy analysis was carried out. Spontaneous dispersion can be achieved when the Gibbs free energy (ΔG_{Mix}) becomes negative for the mixing process between the nanofillers and PVDC. As the calculated mixing entropy (ΔS_{Mix}) using Flory's equation is a very small value, the mixing enthalpy (ΔH_{Mix}) should be extremely small at room temperature to meet the requirement of the equation, i.e., $\Delta H_{\mathrm{Mix}} < T\Delta S_{\mathrm{Mix}}$. The ΔH_{Mix} value depends on the surface energy gap between the PVDC and nanofillers, as shown in equation (1) [22,23].

$$\frac{\Delta H_{\mathrm{Mix}}}{V_{\mathrm{Mix}}} \approx \frac{2}{T_{\mathrm{N}}}(\delta_{\mathrm{N}} - \delta_{\mathrm{sol}})^2 \phi, \tag{1}$$

where the solubility parameter δ_i is the square root of surface energy in phase i ($\delta_i = \sqrt{E^i_{\mathrm{Sur}}}$), T_{N} is the thickness of nanofillers, and ϕ is the volume fraction of nanofillers.

The surface energies of the PVDC matrix and nanofillers were compared based on the contact angle results (Fig. S2 and Table S1). The contact angles of PVDC and nanofillers were analyzed using two different solvents, water and diiodomethane, on their respective films. The water contact angle of neat PVDC was 73.1°, an intermediate value between 35.8° of CNCs and 98.0° of rGOs. When a dual nanofiller system was introduced by nano-patching, the rGO defects were patched with hydrophilic CNCs (Fig. 1b), and the contact angles could be regulated to be similar to that of neat PVDC. For 1C:2R fillers, the contact angles of water and hydrophobic diiodomethane were 74.0° and 21.1°, respectively, which is similar to that of PVDC. PVDC and 1C:2R could consequently result in a negative ΔG_{Mix} owing to similar surface energies facilitating their homogeneous mixing.

As evident from Fig. 2a and b, the dispersion stability of 1C:2R fillers and PVDC/1C:2R nanocomposite [24] was drastically enhanced in the THF and DMF co-solvents. Thus, scalable production of an optically clear film of PVDC/1C:2R can be achieved using the polymer solution casting process. After solution casting, ca. 10 μm thick layer of 0.1 wt% 1C:2R dual nanofiller-incorporated PVDC nanocomposite was transferred on a 125 μm thick PET substrate (Fig. 2c and d). The transparency of the PVDC/1C:2R coated film was measured as 84% at 550 nm wavelength by UV–visible spectrometer in the regular light transmittance mode.

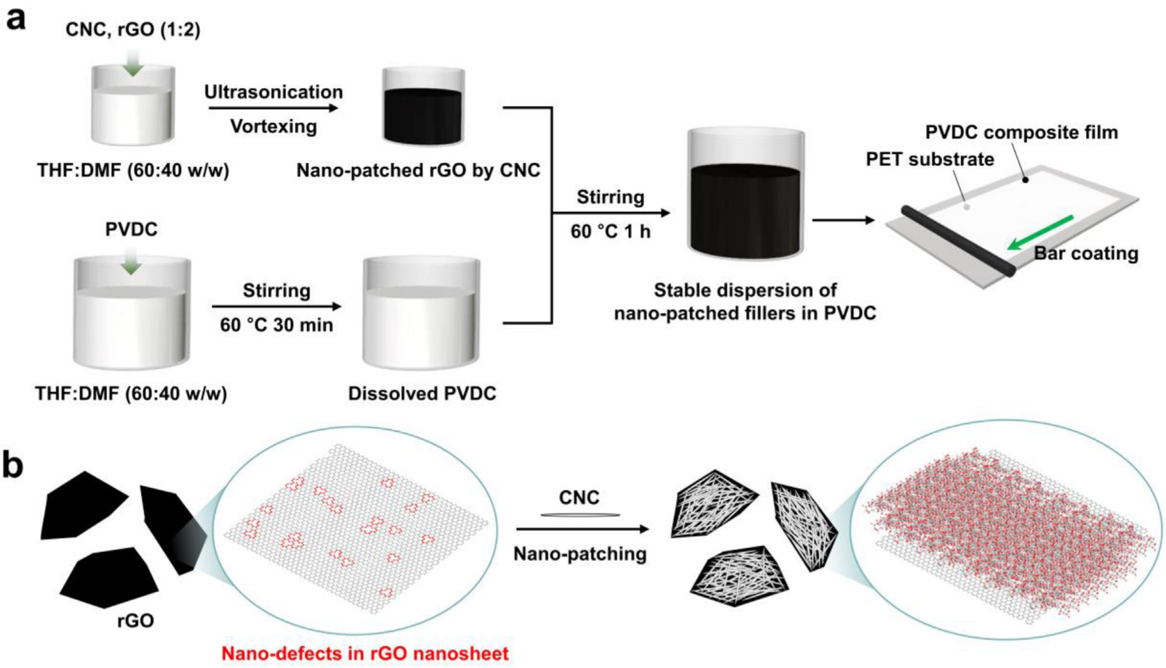

Fig. 1. Nano-patching rGO with CNC in PVDC composites. (a) Schematic dispersion of rGO and CNC nanofillers for PVDC composites. (b) Nano-defects in rGO were patched using CNC. (A colour version of this figure can be viewed online.)

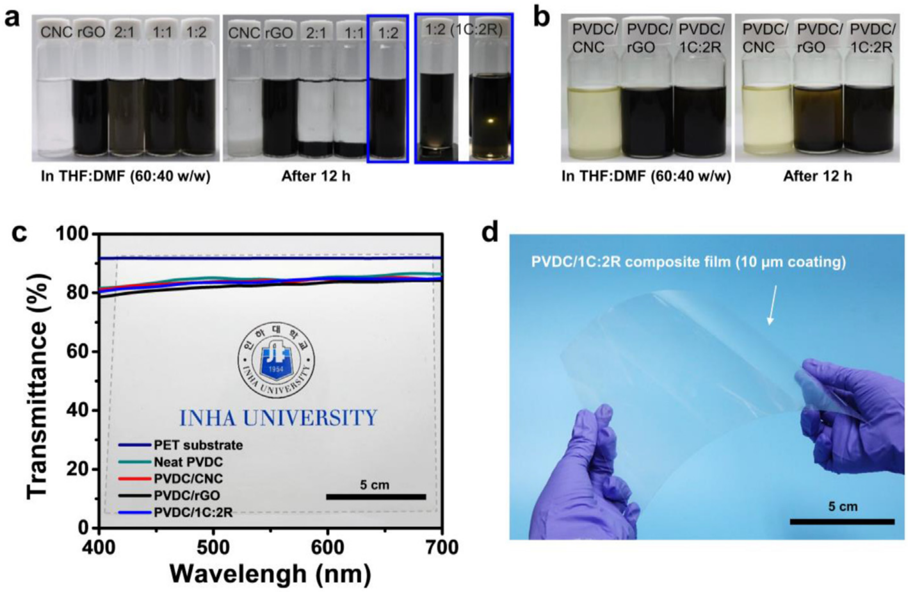

Fig. 2. Dispersion stability of nanofillers. CNC, rGO, and nano-patched 1C:2R fillers in (a) THF:DMF co-solvent and (b) PVDC nanocomposite solutions of 0.1 wt% fillers loading to PVDC. (c) Transmittance results of 0.1 wt% PVDC/CNC, rGO, and 1C:2R nanocomposite films. The 10 μm thick nanocomposite films were deposited on 125 μm thick PET substrates. (d) Large area (17 cm × 21 cm) PVDC/1C:2R–0.1 wt% nanocomposite film was obtained. (A colour version of this figure can be viewed online.)

3.2. Characterization of nano-patched rGO

The hydrogen bonding between the hydroxyl groups of CNCs and oxygen functional groups on the surface of the basal planes of rGO [25] was hypothesized to have led to the homogeneous dispersion and nano-patching effects, which could bridge the gap between the PVDC and rGO interface. The CNCs are one-dimensional needle-like nanowhiskers having a diameter and length of ~20 nm and ~500 nm, respectively, which was confirmed by TEM micrographs (Fig. 3a). Meanwhile, rGOs are two-dimensional nanosheets with lateral sizes of several micrometers and thickness of <20 nm (Fig. 3b). With respect to the 1C:2R fillers, a considerable amount of CNC was adhered on the overall surface of rGO to nano-patch the rGO defects, as shown in Fig. 3c. The presence of favorable intermolecular interactions was further confirmed by densification of the PVDC/1C:2R (Fig. S3). The higher composites density than the theoretical calculation of the rule of mixtures was attributed to the hydrogen bonding between the CNCs and rGO.

To investigate the surface properties of nano-patched systems, XPS experiments were conducted (Fig. 3d and e). In the deconvoluted C 1s spectra of CNCs, a main C–C bond was observed at 284.98 eV along with C–O and C–O–C bonds at 286.48 eV and 288.08 eV, respectively, representing the chemical structure of a typical cellulosic material. In contrast, the C 1s spectra of rGOs showed a large sp^2 C=C bonding peak at 284.38 eV and sp^3 C–C bonding group at 284.98 eV, indicating a defective poly-hexagonal carbon structure including topological defects of rGO. The Raman spectra of rGO revealed a comparable intensity for *D* to *G* band supporting the XPS C 1s data (Fig. S4). As the *D* band originates from the disordered A_{1g} breathing mode of the hexagonal carbon structure, the large intensity of *D* band clearly showed the presence of topological defects. Additionally, the XPS C 1s spectra of rGOs exhibited the C–O bond in hydroxyl groups at 286.48 eV and C=O bond in carbonyl/carboxyl groups at 289.18 eV. Contrary to the oxygen groups of CNCs composed of the main C–O bond and minor C–O–C bond, rGOs consisted of a large number of C=O bonds and a relatively small number of C–O bonds. With respect to the nano-patched 1C:2R fillers, C=O bond of C 1s peaks shifted slightly from 289.18 eV to 289.08 eV, which was associated with lowering of 0.1 eV from 531.98 eV in the O 1s spectrum. The chemical shift to the smaller binding energy of 1C:2R was attributed to the formation of hydrogen bonds between the electronegative oxygen functional groups of rGOs and hydroxyl groups of CNCs.

The nano-patching effect between rGO and CNC was further confirmed by TGA analysis in a nitrogen atmosphere, as shown in Fig. 3f. An initial thermal degradation of 10% weight loss for CNC was exhibited at 132 °C. The dramatic weight loss of CNC at 166 °C was due to dehydration and decomposition of cellulose chains. The rGOs experienced 10% weight loss at 177 °C. The weight loss was more significant in the temperature range from 180 °C to 280 °C, implying pyrolysis of oxygen-containing groups. When CNCs were patched on rGO at a weight ratio of 1:2, enhanced thermal stability revealed strong hydrophilic interactions between CNCs and rGOs. Remarkably, the degradation temperature of 1C:2R fillers at 10% weight loss increased to 230 °C, which is 50 °C higher than the rGO single nanofiller system.

3.3. Characterization of PVDC nanocomposite

To analyze the nano-patching effects of nanoscale rGO defects, the oxygen and water vapor gas barrier properties of PVDC nanocomposites were measured. PVDC matrices were considered for nanocomposite coating films because PVDC features excellent barrier properties against gas and moisture owing to high density and low free volume ratio [26]. The dense molecular structure of PVDC is constructed by highly regular head-to-tail configuration, where two highly polar and electronegative chlorine atoms exhibit a repeating carbon unit of PVDC [27,28]. For polymer nanocomposites, high aspect ratio rGOs are known to drastically enhance the barrier properties owing to the elongated tortuous path of molecular diffusion, as shown in Fig. 4a. When 0.1 wt% high aspect ratio nanofillers were incorporated, the OTR of PVDC/CNC coated film on PET substrates was measured as 1.07 $cm^3\ m^{-2}\ day^{-1}$, which is 42% lower than that of PVDC. The OTR of PVDC/rGO film was measured as 2.3 $cm^3\ m^{-2}\ day^{-1}$, which is 23% lower of that of

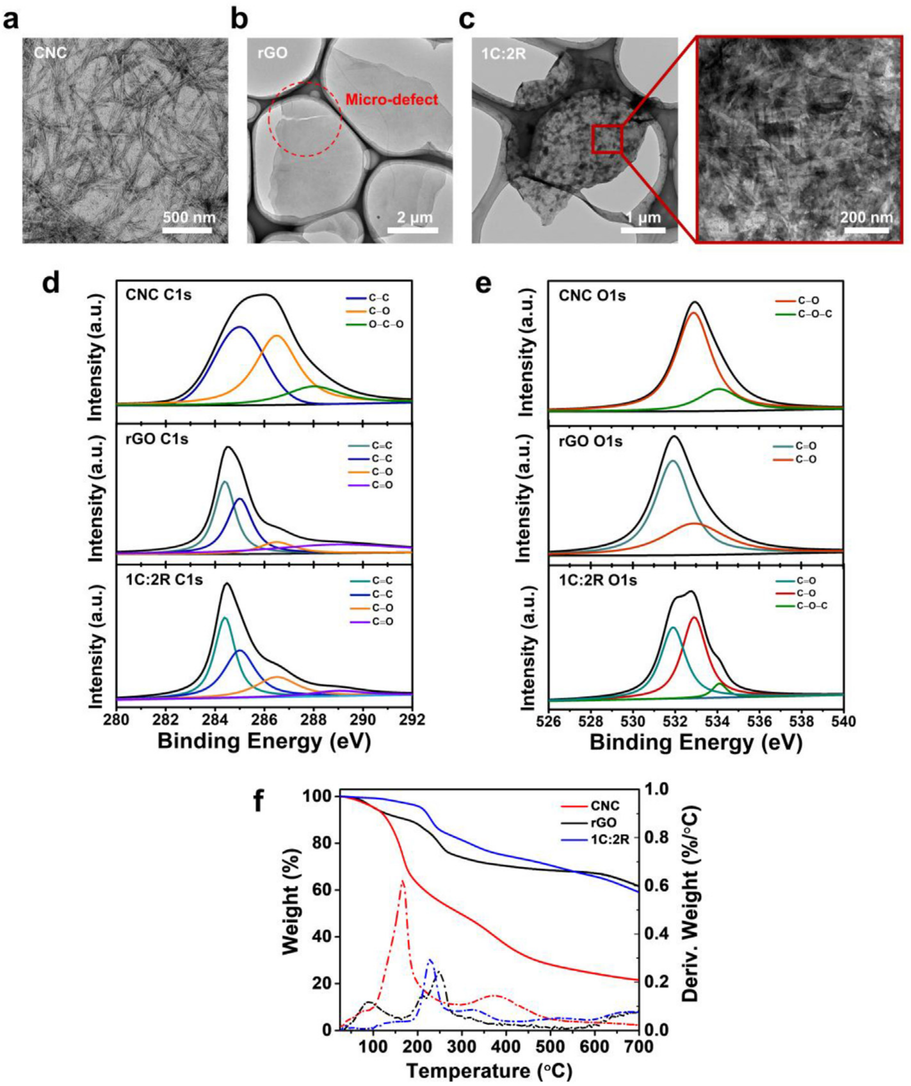

Fig. 3. Hydrophilic interaction of hydrogen bonding between CNC and rGO. FE-TEM micrographs of (a) CNCs, (b) rGOs, (c) 1C:2R. XPS C 1s spectra of (d) CNCs and rGOs; O 1s spectra of (e) CNCs and rGOs. (f) TGA thermograms of CNC, rGO, 1C:2R fillers. (A colour version of this figure can be viewed online.)

neat PVDC film by densification of the PVDC matrices [29] (Fig. 4b). The OTR and WVTR of the PET film substrate were measured as 12.4 $cm^3\ m^{-2}$ day and 4.4 $g\ m^{-2}$ day, respectively. Remarkably, the transparent nano-patched 0.1 wt% PVDC/1C:2R film demonstrated an OTR of 0.45 $cm^3\ m^{-2}\ day^{-1}$, which is approximately 17 times lower than the value of neat PVDC-coated PET film. In addition to the drastically improved oxygen barrier property, the 0.1 wt% PVDC/1C:2R film showed concurrent enhancement of the water vapor barrier property. The WVTR of the 0.1 wt% PVDC/1C:2R film was measured as 0.52 $cm^3\ m^{-2}\ day^{-1}$, while the neat PVDC, PVDC/CNC, and PVDC/rGO films showed the WVTR of 4.3, 0.96, and 0.8 $cm^3\ m^{-2}\ day^{-1}$, respectively (Fig. 4c). This remarkable enhancement of barrier properties was attributed to the nano-patching effects of 2D rGO nanosheets using 1D CNCs. The oxygen functionalities in rGO defects can permeate polar molecules into the free volume of hydrophilic groups. Hence, the defect engineering of rGO using the nano-patching strategy resulted in an effectively hindered permeation of oxygen and water vapor by further increasing the tortuosity in the PVDC matrices.

At elevated temperatures, the poor dimensional stability of the polymeric composites can hinder the reduction of OTR and WVTR due to enhanced segmental mobilities of polymer chains. The thermal expansion of polymer films is characterized by the linear thermal expansion coefficient (CTE) [30] shown below.

$$\alpha = \frac{\Delta L}{L_0 \Delta T}, \tag{2}$$

where α is the linear coefficient of thermal expansion, ΔL is the length change from the initial length of L_0, and ΔT is the temperature deviation. The thermal expansion of the neat PVDC was measured as 348.6 ppm K^{-1} at 77 °C, which was drastically suppressed by the addition of minute amounts of nanoscale fillers (Fig. 5a). As shown in Fig. 5, the addition of 0.1 wt% of CNC or rGO nanofillers reduced the CTE of the PVDC nanocomposites to 294.0 ppm K^{-1} and 229.7 ppm K^{-1}, respectively. The negligible CTE is reported for CNC originating from high crystallinity [31]. For rGO, negative CTE is reported by theoretical calculations and experiments in the temperature ranges of this study (ca. 300–350 K) [32]. For nano-patched fillers, the CTE of PVDC/1C:2R was measured as 271.5 ppm K^{-1} at 77 °C, which is in between the CTE of PVDC/CNC and PVDC/rGO, as expected. Based on the aforementioned

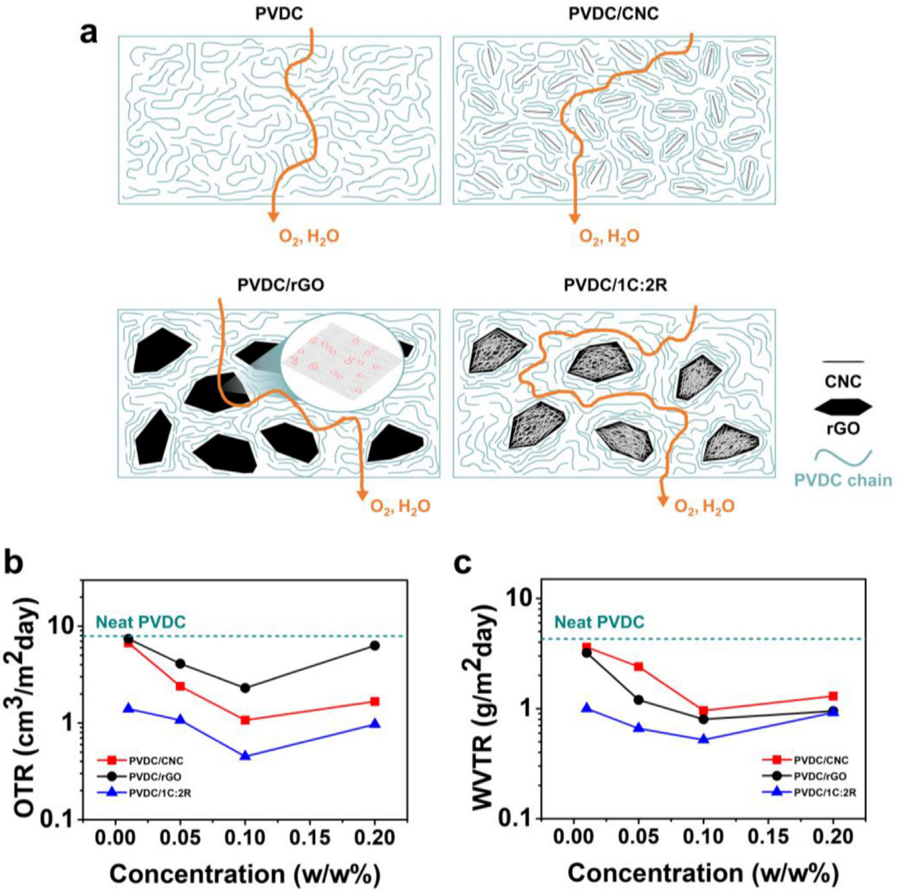

Fig. 4. Barrier properties of PVDC nanocomposites. (a) Diffusion path of oxygen and water vapor in the neat PVDC and filler loading systems of CNC, rGO, and 1C:2R (top-down view), affecting the (b) oxygen transmission rates (OTR) and (c) water vapor transmission rates (WVTR). (A colour version of this figure can be viewed online.)

comparable contact angles resulting from the neat PVDC and PVDC/1C:2R, the effects of hydrophilicity on CTE modification can be excluded. Considering the minute loading of nanofillers, the decrease in CTE is far beyond the prediction from the simple rule of mixtures. Hence, the anomalous CTE suppression is attributed to the nanoconfinement effects at the nanofiller and polymer interfaces [33,34].

In addition to the dimensional stability, thermal decomposition kinetics were investigated upon heating to further elucidate the thermal stability of the nano-patched filler systems (Fig. 5b and Fig. S5). The activation energy for the neat PVDC was measured to be 148.8 kJ/mol based on the Flynn–Wall method by fitting temperatures at isoconversional points using heating rates of 2, 5, 10, and 20 K/min [35]. By including 0.1 wt% of nano-patched rGO by CNC, the activation energy of PVDC/1C:2R increased to 159.1 kJ/mol. This tremendous enhancement with low filler content is attributed to the effective thermal energy transfer via nanoscale interfaces and favorable hydrophilic interactions between the polymer and fillers. As a result, the physically constrained mobility of polymer chains in the PVDC/1C:2R film leads to formation of an efficient barrier when temperature is elevated. Volumetric thermal expansion of polymers is correlated with high segmental mobility in polymer chains. At high temperature, increased free volume in polymer can change the chemical interactions of polymer nanocomposites once water vapor begins to permeate through them. Consequently, these effects of thermal stability on water barrier property were further studied at 0.1 wt% nanofiller loading. The FT-IR spectra of the barrier films were compared before and after water vapor permeation at 40 °C for 3 days (Fig. 5c). Results showed intramolecular hydrogen bonds in the PET substrate coated with PVDC and PVDC composites were affected by the water vapor. Symmetric stretching of the C=O bond at 1713 cm^{-1} and stretching of the C–O bond at 1241 cm^{-1} were exhibited in the PET substrate. Relatively high CTE of the PVDC and PVDC/CNC broadened the band of the C=O bond in the films following water vapor permeation. The C=O bonds at 1708 cm^{-1}, 1710 cm^{-1}, and 1711 cm^{-1} of PVDC, PVDC/CNC, and PVDC/rGO films shifted to 1711 cm^{-1}, 1712 cm^{-1}, and 1713 cm^{-1}, respectively. Significantly, the stretching band of the C=O bond in the PVDC/1C:2R film remained unchanged at 1711 cm^{-1}. The C–O bonds of PVDC at 1237 cm^{-1} and PVDC/CNC at 1240 cm^{-1} were broadened and chemically shifted to 1239 cm^{-1} and 1242 cm^{-1}. The C–O bonds of PVDC/rGO and PVDC/1C:2R film stayed constant at 1239 cm^{-1} and 1240 cm^{-1}, respectively. The thermally stable barrier property against water vapor was induced nano-patched rGO by hydrogen bonding between CNC and rGO. Nanoscale dispersion of the dual nanofillers extends the interface between PVDC and the nanofillers resulting in confined molecular mobility of the PVDC nanocomposite at elevated temperature.

4. Conclusions

The scalable production of transparent PVDC nanocomposite barrier films was achieved using the bar-coating method by incorporating dual nanofillers of rGO and CNC for defect engineering of rGO. The CNC and rGO were solution processed by optimizing the ratio of DMF to THF in the co-solvent system to

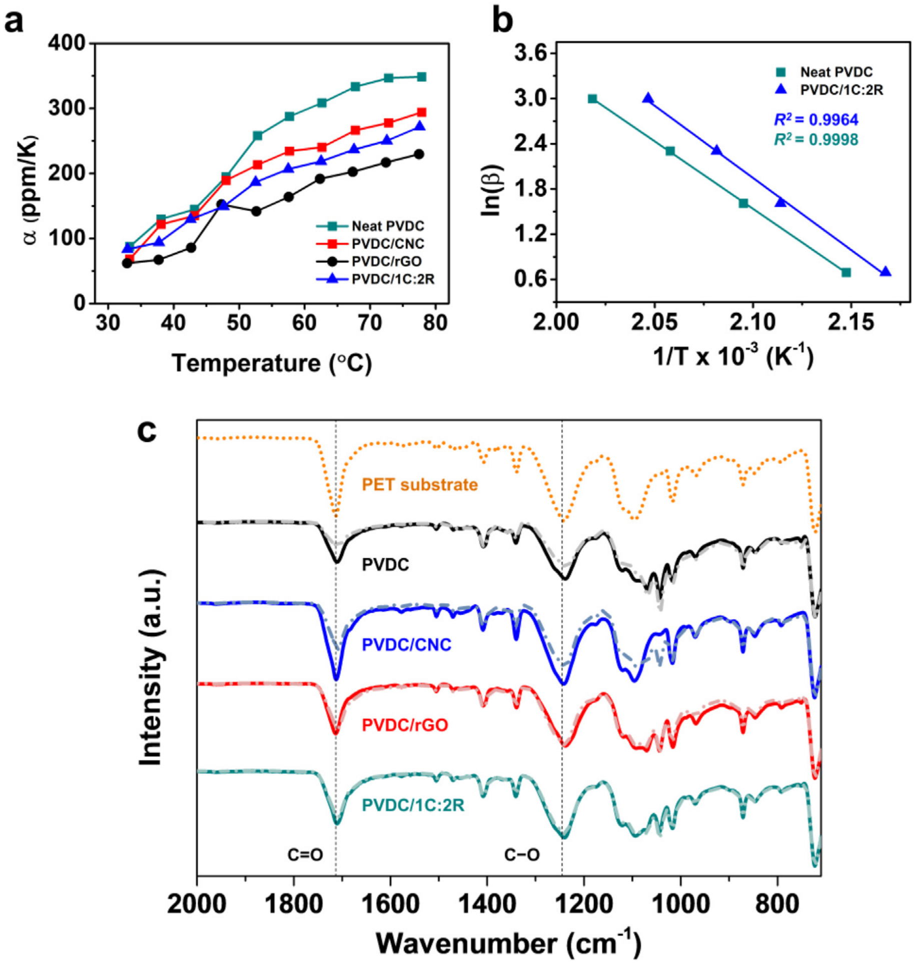

Fig. 5. Thermal stability of the PVDC nanocomposites at 0.1 wt% nanofiller loading. (a) Coefficient of thermal expansion (α) of neat PVDC and nanocomposites at temperatures ranging from 30 °C to 80 °C. (b) Linear plots of natural logarithm of heating rate (β) for neat PVDC and PVDC/1C:2R nanocomposite as functions of inverse temperature (T) in kelvin from the thermal decomposition results by TGA. (c) FT-IR transmission spectra of the barrier films before (dash line) and after the experiments in water vapor permeation at 40 °C for 3 days (solid line). (A colour version of this figure can be viewed online.)

secure dispersibility of the dual nanofillers. The hydrogen bonding between the rGO and CNC prevented the phase separation of CNCs in the organic co-solvent by regulating the surface energy without using the typical aqueous conditions for CNCs. Stable dispersion of the nano-patched rGOs in the PVDC solution enabled the scalable fabrication of optically clear PVDC/1C:2R nanocomposite barrier films by bar-coating. Herein, the defects of rGO were nano-patched through hydrogen bonding between one-dimensional CNC nanowhiskers and two-dimensional rGO nanosheets, as proved by the chemical shifts of XPS binding energy and the enhanced thermal stability from the TGA thermograms. Nano-patching the defective sites of rGO resulted in concurrent improvement of barrier properties against oxygen and water because the highly tortuous diffusion path was secured in the PVDC nanocomposites. The OTR decreased by 17 times and WVTR decreased by 8 times when compared to the neat PVDC coating films. Additionally, the PVDC nanocomposite barrier film revealed the enhanced dimensional and thermal stability that was confirmed by the coefficient of thermal expansion and activation energy for thermal degradation, respectively. Defect engineering of rGO using CNC nanofillers suggests a general strategy to enhance nanocomposite properties of polymer-2D nanosheets, including barrier properties for food and drug packaging.

Declaration of competing interests

The authors declare that they have no known competing financial interests or personal relationships that could have appeared to influence the work reported in this paper.

CRediT authorship contribution statement

Jinhwa You: Methodology, Investigation, Visualization, Writing - original draft. **Sukyoung Won:** Methodology, Investigation, Validation, Visualization, Writing - original draft. **Hyoung-Joon Jin:** Funding acquisition, Project administration, Resources, Supervision, Writing - review & editing. **Young Soo Yun:** Conceptualization, Funding acquisition, Methodology, Project administration, Supervision, Validation, Writing - original draft, Writing - review & editing. **Jeong Jae Wie:** Conceptualization, Methodology, Project administration, Resources, Supervision, Writing - original draft, Writing - review & editing.

Acknowledgments

This research was supported by the Basic Science Research Program through the National Research Foundation of Korea (NRF) funded by the Ministry of Education (NRF-2018R1A4A1025169, NRF-2019R1A2B5B01070270, and NRF-2019R1A2C1084836).

Appendix A. Supplementary data

Supplementary data to this article can be found online at https://doi.org/10.1016/j.carbon.2020.04.024.

References

[1] G. Yuan, D. Lin, Y. Wang, X. Huang, W. Chen, X. Xie, et al., Proton-assisted growth of ultra-flat graphene films, Nature 577 (2020) 204–208.

[2] C. Xiang, P.J. Cox, A. Kukovecz, B. Genorio, D.P. Hashim, Z. Yan, et al., Functionalized low defect graphene nanoribbons and polyurethane composite film for improved gas barrier and mechanical performances, ACS Nano 7 (2013) 10380–10386.

[3] B. Kirubasankar, V. Murugadoss, J. Lin, T. Ding, M. Dong, H. Liu, et al., In situ grown nickel selenide on graphene nanohybrid electrodes for high energy density asymmetric supercapacitors, Nanoscale 10 (2018) 20414–20425.

[4] H.G. Kim, I.K. Oh, S. Lee, S. Jeon, H. Choi, K. Kim, et al., Analysis of defect recovery in reduced graphene oxide and its application as a heater for self-healing polymers, ACS Appl. Mater. Interfaces 11 (2019) 16804–16814.

[5] D. Li, M.B. Müller, S. Gilje, R.B. Kaner, G.G. Wallace, Processable aqueous dispersions of graphene nanosheets, Nat. Nanotechnol. 3 (2008) 101–105.

[6] D.R. Dreyer, S. Park, C.W. Bielawski, R.S. Ruoff, The chemistry of graphene oxide, Chem. Soc. Rev. 39 (2010) 228–240.

[7] D. Konios, M.M. Stylianakis, E. Stratakis, E. Kymakis, Dispersion behaviour of graphene oxide and reduced graphene oxide, J. Colloid Interface Sci. 430 (2014) 108–112.

[8] K. Krishnamoorthy, M. Veerapandian, K. Yun, S.-J. Kim, The chemical and structural analysis of graphene oxide with different degrees of oxidation, Carbon 53 (2013) 38–49.

[9] S. Pei, H.-M. Cheng, The reduction of graphene oxide, Carbon 50 (2012) 3210–3228.

[10] S.-M. Lee, J.-H. Kim, J.-H. Ahn, Graphene as a flexible electronic material: mechanical limitations by defect formation and efforts to overcome, Mater. Today 18 (2015) 336–344.

[11] Y.-X. Shen, W. Song, D. Ryan Barden, T. Ren, C. Lang, H. Feroz, et al., Achieving high permeability and enhanced selectivity for angstrom-scale separations using artificial water channel membranes, Nat. Commun. 9 (2018) 2294.

[12] H.W. Kim, H.W. Yoon, S.-M. Yoon, B.M. Yoo, B.K. Ahn, Y.H. Cho, et al., Selective gas transport through few-layered graphene and graphene oxide membranes, Science 342 (2013) 91–95.

[13] J. Wang, D.J. Gardner, N.M. Stark, D.W. Bousfield, M. Tajvidi, Z. Cai, Moisture and oxygen barrier properties of cellulose nanomaterial-based films, ACS Sustain. Chem. Eng. 6 (2018) 49–70.

[14] J.M. Lagaron, R. Catalá, R. Gavara, Structural characteristics defining high barrier properties in polymeric materials, Mater. Sci. Technol. 20 (2004) 1–7.

[15] A.K. Pal, V. Katiyar, Nanoamphiphilic chitosan dispersed poly(lactic acid) bionanocomposite films with improved thermal, mechanical, and gas barrier properties, Biomacromolecules 17 (2016) 2603–2618.

[16] S.G. Charati, S.A. Stern, Diffusion of gases in silicone polymers: molecular dynamics simulations, Macromolecules 31 (1998) 5529–5535.

[17] K. Choi, S. Nam, Y. Lee, M. Lee, J. Jang, S.J. Kim, et al., Reduced water vapor transmission rate of graphene gas barrier films for flexible organic field-effect transistors, ACS Nano 9 (2015) 5818–5824.

[18] M. Terrones, O. Martín, M. González, J. Pozuelo, B. Serrano, J.C. Cabanelas, et al., Interphases in graphene polymer-based nanocomposites: achievements and challenges, Adv. Mater. 23 (2011) 5302–5310.

[19] J.S. Bunch, S.S. Verbridge, J.S. Alden, A.M. Van Der Zande, J.M. Parpia, H.G. Craighead, et al., Impermeable atomic membranes from graphene sheets, Nano Lett. 8 (2008) 2458–2462.

[20] V.L. Nguyen, B.G. Shin, D.L. Duong, S.T. Kim, D. Perello, Y.J. Lim, et al., Seamless stitching of graphene domains on polished copper (111) foil, Adv. Mater. 27 (2015) 1376–1382.

[21] R. Guzman de Villoria, P. Hallander, L. Ydrefors, P. Nordin, B.L. Wardle, In-plane strength enhancement of laminated composites via aligned carbon nanotube interlaminar reinforcement, Compos. Sci. Technol. 133 (2016) 33–39.

[22] M.Y. Song, Y.S. Yun, N.R. Kim, H.-J. Jin, Dispersion stability of chemically reduced graphene oxide nanoribbons in organic solvents, RSC Adv. 6 (2016) 19389–19393.

[23] Y. Hernandez, V. Nicolosi, M. Lotya, F.M. Blighe, Z. Sun, S. De, et al., High-yield production of graphene by liquid-phase exfoliation of graphite, Nat. Nanotechnol. 3 (2008) 563–568.

[24] Y.H. Shim, K.E. Lee, T.J. Shin, S.O. Kim, S.Y. Kim, Tailored colloidal stability and rheological properties of graphene oxide liquid crystals with polymer-induced depletion attractions, ACS Nano 12 (2018) 11399–11406.

[25] N. Yousefi, K.K.W. Wong, Z. Hosseinidoust, H.O. Sørensen, S. Bruns, Y. Zheng, et al., Hierarchically porous, ultra-strong reduced graphene oxide-cellulose nanocrystal sponges for exceptional adsorption of water contaminants, Nanoscale 10 (2018) 7171–7184.

[26] J.M. Mohr, D.R. Paul, Comparison of gas permeation in vinyl and vinylidene polymers, J. Appl. Polym. Sci. 42 (1991) 1711–1720.

[27] J.L. McClanahan, S.A. Previtera, NMR study of vinyl chloride–vinylidene chloride copolymer, J. Polym. Sci. - Part A Gen. Pap. 3 (1965) 3919–3927.

[28] T. Takahagi, Y. Chatani, T. Kusumoto, H. Tadokoro, Molecular and crystal structure of poly(vinylidene chloride), Polym. J. 20 (1988) 883–893.

[29] J.H. Choe, J. Jeon, M.E. Lee, J.J. Wie, H.-J. Jin, Y.S. Yun, Nanoconfinement effects of chemically reduced graphene oxide nanoribbons on poly(vinyl chloride), Nanoscale 10 (2018) 2025–2033.

[30] X. Shen, C. Viney, E.R. Johnson, C. Wang, J.Q. Lu, Large negative thermal expansion of a polymer driven by a submolecular conformational change, Nat. Chem. 5 (2013) 1035–1041.

[31] J.A. Diaz, X. Wu, A. Martini, J.P. Youngblood, R.J. Moon, Thermal expansion of self-organized and shear-oriented cellulose nanocrystal films, Biomacromolecules 14 (2013) 2900–2908.

[32] D. Yoon, Y.W. Son, H. Cheong, Negative thermal expansion coefficient of graphene measured by Raman spectroscopy, Nano Lett. 11 (2011) 3227–3231.

[33] S.-K. Kim, N.A. Nguyen, J.J. Wie, H.S. Park, Manipulating the glass transition behavior of sulfonated polystyrene by functionalized nanoparticle inclusion, Nanoscale 7 (2015) 8864–8872.

[34] S.-K. Kim, J.J. Wie, Q. Mahmood, H.S. Park, Anomalous nanoinclusion effects of 2D MoS2 and WS2 nanosheets on the mechanical stiffness of polymer nanocomposites, Nanoscale 6 (2014) 7430–7435.

[35] S. Oza, H. Ning, I. Ferguson, N. Lu, Effect of surface treatment on thermal stability of the hemp-PLA composites: correlation of activation energy with thermal degradation, Compos. B Eng. 67 (2014) 227–232.